Scientific Research Publishing

Atmospheric and Climate Sciences, 2021, 11, 614-643
https://www.scirp.org/journal/acs
ISSN Online: 2160-0422
ISSN Print: 2160-0414

On Thunderstorm Microphysics under Urban Heat Island, Sea Breeze, and Cold Front Effects in the Metropolitan Area of São Paulo, Brazil

Isidro Metódio Tuleni Johanes Ihadua, Augusto José Pereira Filho

Universidade de São Paulo, São Paulo-Instituto de Astronomia, Geofísica e Ciências Atmosféricas, Rua do Matão 1226, São Paulo, Brazil

Email: tuleniisidro@gmail.com, augusto.pereira@iag.usp.br

How to cite this paper: Ihadua, I.M.T.J. and Filho, A.J.P. (2021) On Thunderstorm Microphysics under Urban Heat Island, Sea Breeze, and Cold Front Effects in the Metropolitan Area of São Paulo, Brazil. *Atmospheric and Climate Sciences*, **11**, 614-643.
https://doi.org/10.4236/acs.2021.113037

Received: May 12, 2021
Accepted: July 16, 2021
Published: July 19, 2021

Abstract

This work discusses issues related to the impact of urbanization on the microphysical processes of precipitating systems associated with synoptic, mesoscale, and local scale systems. Among the issues addressed is the impact of urban heat island (UHI) in São Paulo city center and urban densification (UD) in the Metropolitan Area of São Paulo (MASP) on the microphysical, dynamic, and thermodynamic properties and distribution of precipitation and heavier rainfall from sea-breeze (SB) e cold-front (CF) combined during their space-time evolutions. For this purpose, it used four components: classification of hydrometeors with fuzzy logic, calculation of the raindrop diameters, an estimate of liquid water mass and ice mass from polarimetric-variables measured with dual-polarization X-band meteorological radar. The results indicated that urban densification (UD) and heat island (UHI) of the São Paulo city center impact the formation of precipitation, liquid water mass, and ice mass, depth, and duration of a thunderstorm. It was also observed the asymmetric configuration of the thunderstorm is induced by the strong convergence in the São Paulo city center, and this strong convergence is induced by the intense heat island (UHI) in the São Paulo city center. Was also observed that this event that is formed in the Metropolitan Area of São Paulo (MASP) depends on microphysical processes of mixed-phase of the cloud (water and ice) above the 0˚C isotherm for the production of intense rain and cold pool at the surface. These important microphysical processes within long-lasting secondary convective cells over the São Paulo city center should be taken into account on convective parameterization schemes as well as the associated cold pool dynamics.

Keywords

Weather Radar, Fuzzy Logic, Sea Breeze, Urban Densification, Hail, Asymmetric Thunderstorm Configuration

1. Introduction

The Metropolitan Area of São Paulo (MASP) is among the five largest megacities of the planet. The diurnal cycle of surface diabatic heating, induced local circulation in an aerosol-rich environment is the main ingredients of deep thunderstorms in MASP [1]. The MASP is recurrently affected by flash floods, mudslides, heavy winds, lightning, and hail that cause significant social and economic impacts [2].

The geometric center of MASP is different from suburban surroundings in both material and geometry, with multiple intersecting paved roads, impervious surfaces and denser irregular constructions in urban areas causing the heat island (UHI) of the São Paulo city [1]. About 70% of all severe weather events within MASP were associated with local circulation induced by topographic and UHI effects [3]. The SB is the most common local circulation. In midafternoon hours while the SB front pushes continent ward from southeast against prevailing northwest winds (approaching CF), injecting a deeper layer of moisture over the MASP warmer and drier urban boundary layer, often causing major flood episodes [4]. The UHI is caused by large sensible heat storage within the urban canopy in the early hours of the day and released during the afternoon and night over the center of the MASP [1].

The SB fronts tend to increase environmental shear and associated vorticity and moist [5] and MASP urban aerosol convergence [2]. When the SB front and gust fronts of the primary cells collide there is a reduction of moist static stability and new convective cells initiate over the center of the MASP [6]. According to [7] the UHI forms a strong convergence zone in the center of the MASP and thereby accelerates the SB front toward the center of the MASP. After it arrives in the urban region, the SB front stalls over the MASP for 2 h. Subsequently, the sea breeze progresses beyond the city when the heat island dissipates. Thereafter, the SB front propagates beyond the urban area at a decelerated rate. The effects of the UHI on convective cell initiation and thunderstorm, resulting in the temperature contrast as a condition for storm initiation over the MASP [8]. The UHI effects amplify the thunderstorm activity by local factors (sea and country breeze, synoptic events, and terrain) and the higher flash rates throughout the urban region, which influences the lightning density in the MASP [8].

Under these local circulations and aerosol effects, microphysical processes tend to play an important role in the dynamics and thermodynamics of thunderstorms in MASP [9] [10] [11]. [12] analyzed measurements of drop size distribution in two thunderstorms in MASP. According to [12], the effects of the urban aerosol load were the factor affecting the deep convection of two thunderstorms (lower aerosol load and higher aerosol load) of the SB events. The thunderstorms associate with the higher aerosol load (on January 11, 2010) longer-lasting convection and larger raindrop concentration than the one observed in the Amazon Forest during LBA [11] [12]. [11] reported about the thunderstorm (on January 11, 2010) caused by synoptic conditions and typical deep SB circulation

over MASP. The CF moved through over South Brazil which intensified northwest circulation and convergence against the SB front midafternoon. This scenario triggered thunderstorms under a moist unstable environment and strong convergence over MASP.

In the most intense urban heat island conditions on the polluted MASP occurs deep storms that depend on the humidity provided by the sea breeze and the prefrontal flows over the MASP, which caused flooding and other severe climatic characteristics on January 11, 2010. The amount of rain recorded was 177.3 mm, 68.7% of the historical average for January which is 258 mm [11]. The state of São Paulo was with the twenty-one (21) cities in an emergency and two (2) in a public calamity situation, caused by a sequence of 11 days of heavy rains in January 2010. In MASP it rained almost 70% of the total precipitation of January between days 1 and 12. This SB event was associated with the interaction of MASP heat island and CF and caused a high accumulation of rain. According to the INMET (2010), wind gusts reached 60 $km \cdot h^{-1}$ in Osasco City (west MASP) caused by the thunderstorm on 11 January 2010. In addition to the wind damage, the heavy rain caused flash floods in MASP.

However, observational studies, modeling, surface data, and remote sensing estimates by meteorological radars and satellites were conducted to better understand the dynamics of SB and CF interaction with local circulations induced by the presence of MASP. The processes by which convection starts and is organized were understood to adequately represent the daytime precipitation cycle in numerical models [5] [7] [11] [13]. But the evolution of microphysical processes must be studied to provide a physical basis for estimating precipitation by remote sensing [14]. Hydrometeor classification using polarimetric radar data provides detailed information to validate and improve microphysical and convective parameterizations. Microphysical information is known to significantly affect local and mesoscale numerical models [15] [16]. Therefore, microphysical effects are of extreme relevance for understanding the behavior of convective episodes [17].

Microphysical knowledge of thunderstorms is vital because, in recent decades, damage caused by these events seems to have increased because of urban microclimatic changes due to anthropogenic actions. The impact of severe convention episodes can be minimized by accurately predicting, saving lives, and preventing economic losses [18].

The MXPOL weather radar measurements detected with high spatial-temporal resolution the penetration of the sea breeze at MASP where the heat island was already intense. The satellite image sequences showed the arrival of the cold front over MASP at the same time with penetration of the sea breeze which probably caused hail precipitation and microbursts at one end of the storm. Thus, this work was motivated to analyze the microphysics of a rare event induced by the combination of systems of different scales on January 11, 2010, that, eventually, the microphysical inference can provide information for parameterizations of cloud and mesoscale models.

2. Study Area, Dataset, Instrumentation, and Microphysics Analyses

The study was performed over the Metropolitan Area of São Paulo-MASP (Figure 1). The MASP is a megacity environment composed of 39 cities [19]. It has been increasing in vertical growth with very limited vegetated areas in the São Paulo city. The MXPOL was strategically placed to the west of São Paulo city to monitor the propagation of sea breeze fronts. The Joss-Waldvogel disdrometer (JWD) was placed approximately 30 km away from the MXPOL (Figure 1(a)). Figure 1(b) shows a visible satellite image of MASP and its surroundings. It is quite remarkable the color contrast between the MASP surface (brownish) and its ocean (blueish) and rural (greenish) surroundings (Figure 1(b)).

The land cover change (brownish) caused by anthropogenic action through the last century has resulted in drastic changes in its energy and water budgets in MASP (Figure 1(b)). About 70% of all severe weather events within MASP were associated with local circulation induced by topographic and UHI effects [2].

2.1. Technical Features of the MXPOL

MXPOL is a mobile X-band (9.37 GHz), dual-polarization Doppler weather radar system switchable to single polarization mode with a maximum of 601 gates at 150 km range. In horizontal-only transmitted mode with a longer pulse length, the sensitivity of the radar is better than 3 dB when compared to a dual-polarization mode of operation. In the horizontal-only transmitted mode, the dual-channel receiver is capable of measuring both co- and cross-polarized backscattered signals. Table 1 shows the technical characteristics of the MXPOL antenna, pedestal, transmitter, and receiver reflector. The volumetric scanning strategy for 11 January 2010 was a clockwise azimuth scan low to high elevation angle at a 5-minute time interval (0.6˚, 1.2˚, 2˚, 3˚, 4.5˚, 6˚, 9˚, 12˚, 16˚, 20˚, and 25˚). The collection of successive PPIs (Plan Position Indicator) of the radar is a

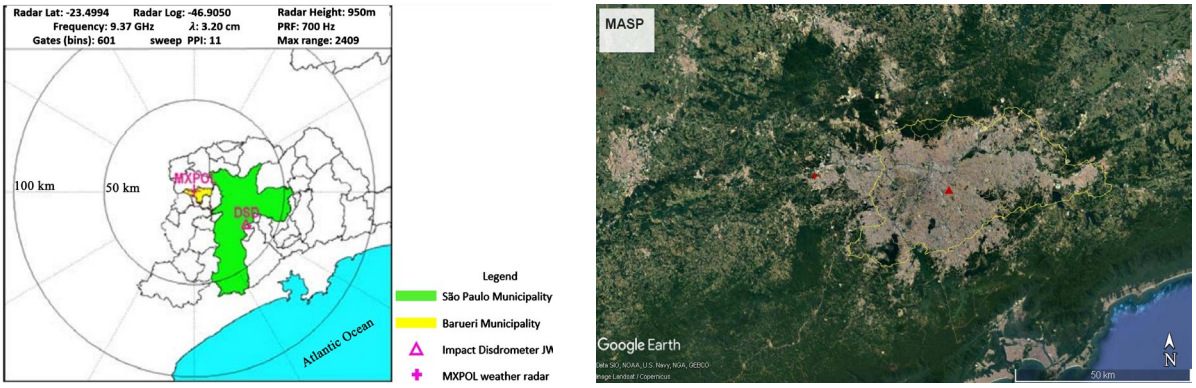

(a) (b)

Figure 1. (a) MXPOL surveillance area in the MASP. Cross and triangle indicate the location of MXPOL (23º 32.2' S; 46º 52.8' W) and the JWDat Parque Estadual Fontes do Ipiranga (PEFI), respectively. Green and yellow areas are São Paulo and Barueri Cities, respectively. (b) The yellow line indicates the boundary of the Metropolitan Area of São Paulo (MASP). Red star and triangle indicate MXPOL and JWD locations. (a) Source: Adapted from [19].

Table 1. Technical characteristics of the MXPOL weather radar system. Source: adapted from [1].

Transmitter	Reception
Magnetron	Two digital channels (H, V)
Frequency of 9.4 GHz	Radar Noise Figure < 2.5 dB
Peak power 80 KW	Dynamic range (H, V) > 80 dB
Pulse modulation	ADC 14 bits
PRF 500 to 5000 Hz	Local oscillator DAFC
Linear polarization (H, V) simultaneous	MDS (H, V) 113 dBm at 2 μs
Solid state modulator	
Duty cycle 0.001	
Pedestal	Reflector
Azimuth scan 00 to 3600	Parabolic
Elevation scan 00 to 900	Diameter 2.44 m
Maximum scan 360 s^{-1}	Antenna Gain 44 dB
Pointing imprecision < 0.10	HPBW at 3 dB < 100

volumetric scanning.

Radar is one of the best tools available for monitoring and forecasting as it provides real-time monitoring with height spatial resolution and allows a three-dimensional view of the data [20]. The radar consists of a transmitter, a receiver, an antenna, and a decoding and processing system (**Table 1**). Radar is a remote sensing tool, that is, through electromagnetic radiation, collects data without coming into direct contact with the study target.

Data collection occurs when the radar transmits a beam of electromagnetic radiation and captures the energy reflected by the particles present in the atmosphere. This energy is amplified and, given the time interval between emission and echo return, it is possible to determine the distance from the target to the radar and to describe the hydrometeors types.

The following variables, obtained from MXPOL volume data were used in this study:

Reflectivity (Z). The Z is the measure of a target's efficiency in intercepting and returning the energy emitted by the radar. Thus, reflectivity is dependent on the sizes, formats, quantity, and dielectric properties of the targets [21]. High reflectivity values (up to 45 dBZ) are generally associated with heavy rainfall, if these values are between 5 and 12 km of altitude, they are associated with severe storms [22].

Radial velocity (V). The V is how fast the detected target is moving away or approaching the radar. Using the Doppler effect, the radar estimates the velocity at which the target moves toward or moves away from radar [21]. By convention, blue tonality (negative values) represents particles coming toward the radar, and red tonality (positive values), particles moving away from radar [22].

Differential Reflectivity (Z_{DR}). The Z_{DR} is the difference between Z_{HH} (reflec-

tivity with the signal emitted and captured horizontally) and Z_{VV} (reflectivity with the signal emitted and captured vertically) [21]. The variable Z_{DR} is widely used to differentiate rain, hail, snow, and even non-meteorological targets [23].

Phase Differential (PHIDP). The PHIDP is the difference between the phase emitted and received horizontally and the phase emitted and received vertically in a pulse [22]. The variable PHIDP has radial variations, since cumulative changes in the phase difference for the complete pulse journey.

Specific Phase Differential (K_{DP}). The K_{DP} variable is the spatial derivative of PHIDP and is an excellent estimator for precipitation, as presented by [24], values above 2˚/km indicate a significant amount of liquid or oblate water.

Copolar Correlation (RHOHV). The RHOH represents the correlation between the horizontal and vertical polarized Z signals at a given point in space [20]. The values of RHOHV vary between 0 and 1.0 and can be seen as a measure of the similarity between horizontal and vertical polarization signals [23]. This variable describes the physical characteristics of the target, being closer to 1.0 the more uniform the target since the vertical and horizontal signals tend to be the same.

The data collected by the MXPOL are in spherical coordinates, where the position of each data is described in terms of (θ, φ, r), where θ is the angle of antenna elevation, φ is the angle of clockwise rotation of the antenna relative to the geographic North, called the azimuth angle, and r is the distance from the radar to target.

2.2. The MXPOL and JW Disdrometer Datasets

The 11 January 2010 thunderstorm microphysics was analyzed through Dual Doppler polarization (DDP) band X radar and JW disdrometer data. Five hours of polarimetric data namely, the reflectivity of horizontally polarized waves Z_H; differential reflectivity Z_{DR}; specific differential phase K_{DP}; and correlation coefficient between horizontally and vertically polarized signals ρ_{HV} were used in the microphysical analyses through the supervised fuzzy logic method during the spatial-temporal evolution of the storm. Three and half hours of JW Disdrometer (JWD) data were used for droplet spectrum analysis during the spatial-temporal evolution of the storm.

Hydrometeor types were mapped on PPIs to analyze the thunderstorm mixed-phase microphysics. Datasets were selected under MASP heat island, polluted conditions, SB, and CF effects. The above MXPOL polarimetric variables and respective vertical temperature profiles were input to the hydrometeors classification (HC) method and then visually verified against typical hydrometeor polarimetric signatures.

2.3. Hydrometeor Classification (HC)

The fuzzy logic method is a technique for synthesizing information from polarimetric variables into a hydrometeor classification algorithm [25]. We used the fuzzy logic hydrometeor identification algorithm for XPOL radar data developed by [26].

Four polarimetric variables (Z_H, Z_{DR}, K_{DP}, and ρ_{HV}) from MXPOL radar and local altitude (temperature) were used as input data for hydrometeor classification of precipitating systems using the fuzzy logic method. Temperature (˚C) and height (m) data from the radiosonde of Campo de Marte aerodrome were interpolated for each grid point at each PPI. The interrelations of polarimetric variables and altitude generated information for automatic identification of the hydrometeors represented at each PPI grid point.

- Python ARM Radar Toolkit (Py-ART)

The Python ARM Radar Toolkit (Py-ART), an open source library for working with weather radar data [27]. Py-ART was used to read and visualize the polarimetric MXPOL weather radar data and perform the hydrometeor classification using the fuzzy logic method, calculate the raindrop diameter (D_0), the solid water mass and the liquid water mass at each grid point in all the IPPs and generate graphs with the algorithms available in the CSU Radar Tools platform developed by [25]. The algorithms are implemented in modules such as Scientific Python, including NumPy, SciPy and matplotlib and Python to realize the interface with weather radar polarimetric variables with radiosonde data, etc, and computationally accelerate their execution.

- The fuzzy logic method

The HC in the thunderstorm was performed using the Fuzzy logic method using python programming language [27]. This method uses smoother transitions within the limits of the observed polarimetric variables, for each type of hydrometeor and simple rules rather than analytical equations to describe the system in question [25]. This method is used to decide on the right output class-based on 4 input polarimetric variables and temperature (**Figure 2**). HC was carried out discriminates several types of hydrometeors for X-pol based on weather radar measurements, T-matrix simulations and Mueller-matrix scattering models aiming at defining membership beta functions (MBFs) implemented by [28].

Figure 2 shows the implemented structure of the fuzzy logic algorithm consisting of four steps [29] and the typical values used for dual-pol variables are shown in **Table 2**. The algorithm uses the associated predefined functions to automatically classify the multidimensional input data. The classification was applied at each gate of the weather radars such that a complete field of hydrometeor type was produced consistent mainly with the polarimetric data of the SPOL radar. The hydrometeor types were mapped as a PPI for microphysical analysis during the spatial-temporal evolution.

Table 2 contains the hydrometeors types corresponding to the thresholds of the Z_H, Z_{DR}, K_{DP}, ρ_{HV}, and temperature.

The method is robust enough that its performance cannot be affected due to typical measurement error in some of the input variables [30] [31]. This procedure is reliable for automatic classification and is most suitable for hydrometeor classification [28].

The fuzzy-logic method consists of four major components (**Figure 2**): fuzzification,

Table 2. Hydrometeor types corresponding to the thresholds of the Z_H (dBZ) reflectivity, Z_{DR} (dB) differential reflectivity, K_{DP} (km^{-1}) specific differential reflectivity, ρ_{HV} correlation coefficient, and altitude data. Source: [29].

Hydrometeors Types	Polarimetric variables/Altitude				
	ZH (dBZ)	*ZDR* (dB)	*KDP* (*o* km^{-1})	*RoHV*	Temperature (˚C)
Drizzle	0 to 25	0 to1	0 to 0.1	0.99 to 1	0 to 45
Rain	24 to 56	0.3 to 5.6	0.3 to 6	0.95 to 0.98	0 to 45
Graupel LD	28 to 45	−0.9 to 1.6	0.3 to 6	0.89 to 0.98	−45 to −5
Graupel HD	35 to 52	−1 to 3.1	−1.8 to 4.8	0.90 to 0.98	−10 to 5
Wet snow	5 to 58	0.5 to 2.5	<−2 to 2	0.75 to 0.97	−0.2 to 0.2
Aggregates	2 to 30	0.3 to 1.3	−0.4 to 0.9	0.96 to 0.99	−45 to −5
Ice crystals	<0 to 18	0.8 to 5.8	0 to 0.3	0.96 to 0.98	<−48 to −5
Ice vertical	<0 to 22	−1.8 to −0.2	−2 to −0.5	0.95 to 0.98	<−48 to −5
Hail	50 to >65	−0.3 to 0.5	−0.4 to 1.8	0.76 to 1	−30 to 30
Big drops	48 to 68	2.8 to 6	0.2 to 6.5	0.95 to 0.98	0 to 48

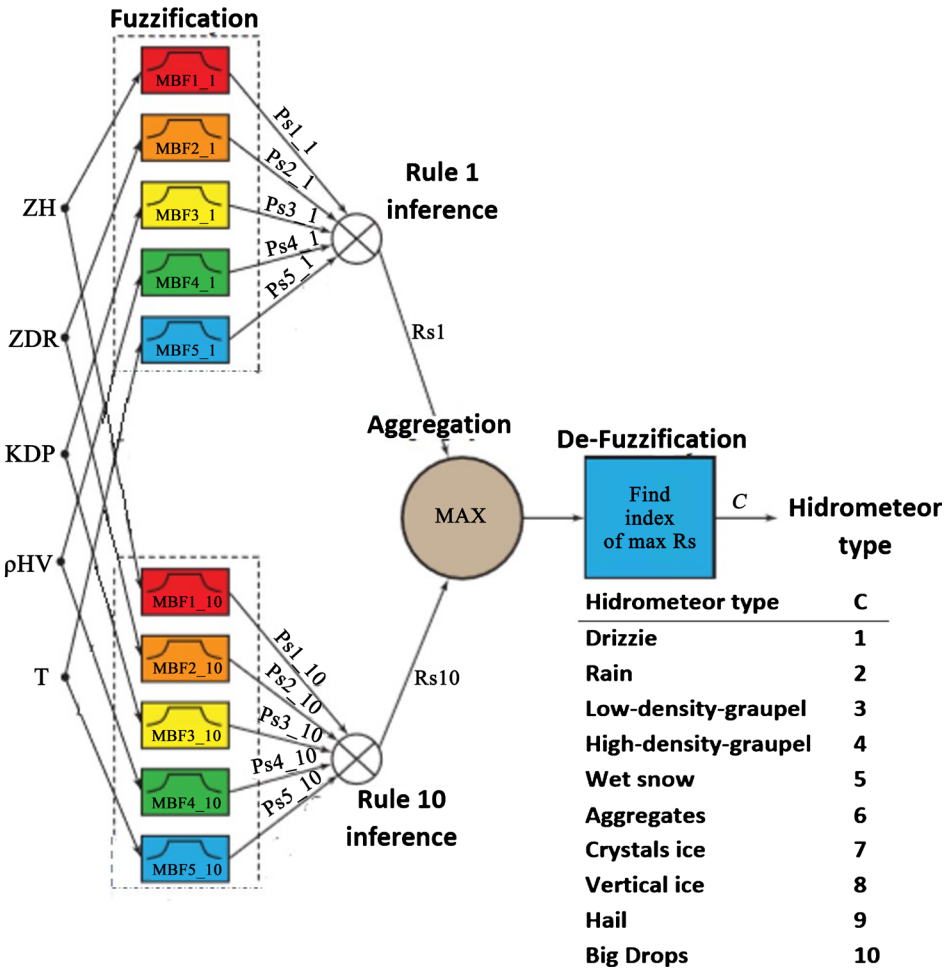

Figure 2. Illustration of a fuzzy logic hydrometeor classification algorithm developed by [28]. Adapted from [29].

inference rule, aggregation, and defuzzification [28].

Fuzzification: fuzzy logic schemes transform discrete data into Fuzzy sets with their corresponding weight. A specific input variable may belong to different Fuzzy sets, but also with different weights. The most important component of this step is the "member function" [28], which is used to describe the relationship between input data and the fuzzy set. During the fuzzification of each variable, all hydrometeors receive a value between 0 and 1 through the member function (MBFs), which is the degree to which that hydrometeor is related to the fuzzy set it belongs.

Inference: in a Fuzzy logic system, rules are used to describe the relationship between input and output fuzzy variables in Boolean form, that is, if the input data is x, then the output data must be y [28]. The degree of importance's rules within the Boolean form can be determined by a series of methods, such as minimum correlation, product correlation, and minimum-maximum relationship [28]. The result of fuzzification is multiplied by a predetermined weight, a value that is determined by its usefulness in classifying and measuring the accuracy of input variables.

Aggregation: inference methods can be used to calculate the weight of each rule, so the aggregation method is used to determine the entire Fuzzy space to be analyzed. The values obtained by the inference rule are then aggregated to form a single value for each Fuzzy set, that is, hydrometeor or hydrometeor set.

Defuzzification: the output of the aggregation process is a fuzzy value. In many applications, such as hydrometeor classification, it is necessary to find a discrete output value that best represents the fuzzy output value, so the data is transformed into dimensional space. The average of the maximums that "defuzzify" the data and determine the strength of each fuzzy set, defined by this value the class of hydrometeors that it belongs to. In addition, it generates an output field, where the hydrometeors are classified into 10 categories (**Figure 2**).

- Membership functions (MBF)

The MBF determination is an important step of the fuzzy-logic-based HC method. [31] Developed the parameters and the membership functions for X band polarimetric variables for each hydrometeor that was used in this work, by the following equation:

$$BF = \frac{1}{1+\left[\left(\frac{x-m}{a}\right)^2\right]^b} \tag{1}$$

where

x = polarimetric variables;

m = center;

a = width;

b = slope.

Table 3 contains the parameters set of the membership functions for four polarimetric variables and temperature for each hydrometeor type used in Equation (1).

- Estimates of mass of liquid water, the mass of solid water, and mean droplet diameter.

The methodology of [32] was applied for the estimates of liquid water mass and solid water mass [26]. The mass of ice and water was calculated at specified height levels, given Z_H and Z_{DR} at each grid point [28] from the following Equations:

$$M_w = 0.70\times10^{-3}\left(Z_H^{0.886}\right)\left(\varsigma^{-4.159}\right)\left(\mathrm{g\cdot m^{-3}}\right), \quad (2)$$

where

$$\varsigma = \frac{Z_H}{Z_V} = 10^{Z_{DR}/10}, \quad (3)$$

Z_H = horizontal reflectivity of the hydrometeor classified as rain ($\mathrm{mm^6\cdot m^{-3}}$);
Z_V = vertical reflectivity of the hydrometeor classified as rain ($\mathrm{mm^6\cdot m^{-3}}$);
Z_{DR} = differential reflectivity of hydrometeor classified as rain (dB).

$$M_i = 1000\pi\rho_i N_0^{3/7}\left(\frac{5.28\times10^{-18}Z_H^{ice}}{720}\right)^{4/7}\left(\mathrm{g\cdot m^{-3}}\right), \quad (4)$$

where

Z_H = horizontal reflectivity ($\mathrm{mm^6\cdot m^{-3}}$) of the hydrometeor classified as ice;
ρ_i = ice density (0.917 $\mathrm{kg\cdot m^{-3}}$);
N_0 ($4\times10^6\ \mathrm{m^{-4}}$) = intercept parameter of an assumed exponential inverse distribution for ice [28].

To calculate the mean raindrop diameter, the following relationship obtained by [32]:

$$D_m = 1.619 * Z_{DR}^{0.485}. \quad (5)$$

Table 3. Membership functions for polarimetric variables for rain, drizzle, big drops, ice crystals, aggregates, hail, low-density graupel, high-density graupel, wet snow, and vertical ice for hydrometeor identification algorithm. Source: [28]. Accessed on October 23, 2018.

Hydrometeor Types	Membership functions (MBFs)														
	Temperature			K_{DP}			Z_H			Ro_{HV}			Z_{DR}		
	m	*a*	*b*	*m*	*a*	*b*	*m*	*a*	*b*	*m*	*a*	*b*	*m*	*a*	*b*
Drizzle	4.0	4.1	5.0	0.03	0.03	2	2	29.0	10	1.0	0.015	2	0.45	0.45	5
Rain	4.8	5.1	3.0	12.75	13.00	6	42	17.0	10	1.0	0.040	2	2.85	3.02	9
Graupel LD	−5.0	5.0	2.5	0.70	2.10	3	36	9.0	8	1.0	0.016	1	0.30	1.00	6
Graupel HD	−2.5	2.0	2.0	1.55	3.05	3	43	9.0	5	1.0	0.035	1	0.60	1.15	2
Wet snow	1.0	3.5	5.0	−7.00	8.10	6	28	29.0	10	0.7	0.260	10	1.60	1.20	10
Aggregates	−2.5	2.6	1.5	0.20	0.20	1	16	17.0	15	0.91	0.020	3	0.70	0.70	7
Ice crystals	−5.0	5.0	2.5	0.15	0.15	6	−3	22.0	20	1.00	0.030	3	3.20	2.60	10
Ice vertical	−5.0	5.0	2.5	−0.79	0.79	3	−3	22.0	20	0.98	0.020	3	−0.90	1.00	10
Hail	0	10	5.0	0.50	1.50	6	59	10.3	6	0.97	0.150	3	0.12	0.50	8
Big drops	4.8	5.1	3.0	3.60	3.30	6	56	9.0	10	0.98	0.030	3	4.30	1.00	8

3. Results

3.1. Synoptic Analysis

The IR satellite images (Figure 3) show the displacement of a CF towards the southeastern region. Where it is observed the most intense cloud band extremity over the Santa Catarina and Paraná states at 1600 UTC (Figure 3(a)) and the eastern part of the São Paulo state is covered with warm cloud of prefrontal system.

However, Figure 3(b) shows an intense cloud-band moving towards MASP (1730 UTC, highlighted area), that might be associated to the sea breeze front. Figure 3(c) shows that part of the eastern region of the São Paulo state is cloud-covered, but except MASP (2000 UTC), already with the SB front over the center of MASP. The cloud-band is asymmetrically configured because of the blocking of the SB-front by intense MASP heat island and northwest winds.

This SB-front is temporarily stagnant over the center of MASP caused by the intense MASP UHI. At 2100 UTC, while the SB-front moves outside MASP push continent ward from southeast against prevailing northwest winds, injecting a deeper layer of moisture over the MASP warmer and drier urban boundary layer, causing a deep cloud trigger (highlighted area).

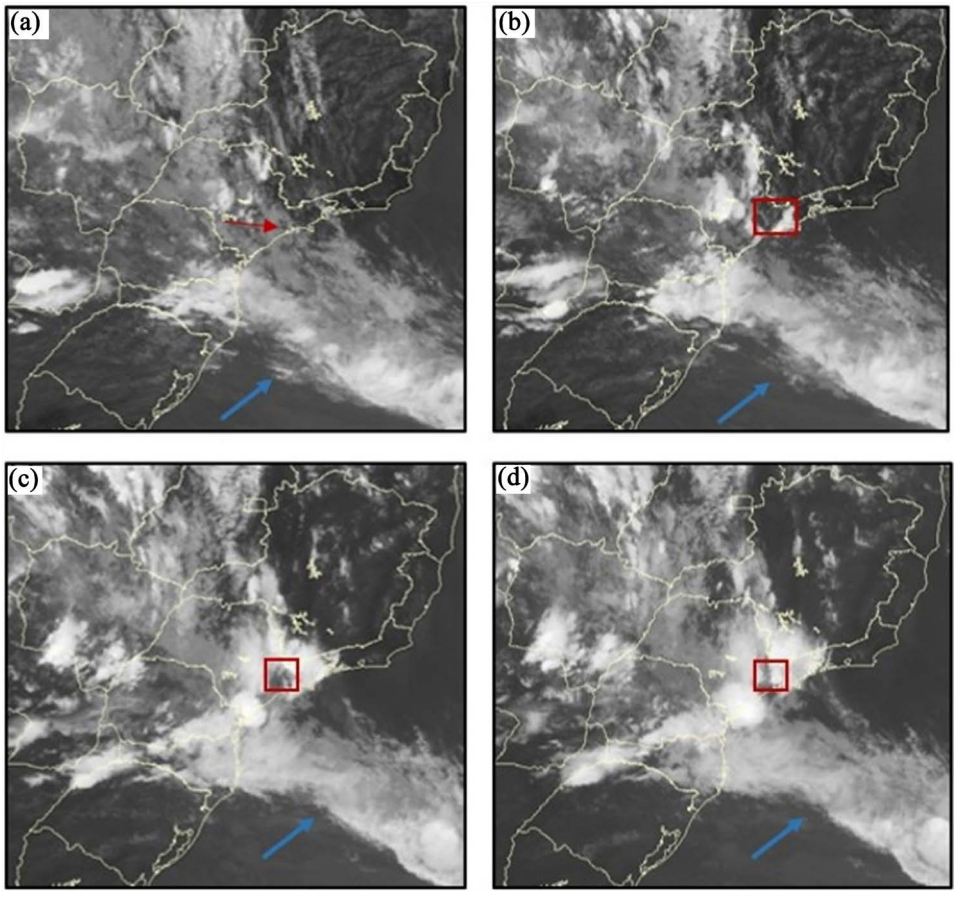

Figure 3. GOES-12 infrared 4 channel (a) 1600 UTC, (b) 1730 UTC, (c) 2000 UTC and (d) 2100 UTC on 11 January 2010. The blue arrow indicates the cold front position and the red square and arrow indicate the MASP region. Source: DSA-CPTEC.INPE, 2010.

3.2. Thermodynamic and Dynamic Analysis

Figure 4(a) shows the temperature, humidity, and wind profile measured with the radiosounding at Campo de Marte Airport (23˚30'31"S, 46˚38'15"W) at 1200 UTC on January 11, 2010.

It shows a very high mixing ratio between 700 - 800 hPa in almost all troposphere. It is observed a strong entanglement of dry and hot air mass between 450 hPa and 700 hPa of medium atmosphere, which favors the deep mixing of the boundary layer, causing strong updrafts that carry moisture to the tropopause. These thermodynamic conditions strengthen convective cells [33].

The CAPE indicated 1491 J·kg^{-1} and Lifted index of −4˚C (Figure 4(a)). The superficial heating during the day and the injection of moisture in the afternoon (Figure 4(a)), increased the instability indexes in an environment of weak vertical shear.

Figure 4(b) shows the vertical moisture profile cross-section at longitude 47 ˚ 60'W from latitudes 22 ˚25'S to 24 ˚95'S of MASP at 1800 UTC on January 11, 2010. A moisture layer is observed varying between 60 - 90 to tropopause over the MASP during the SB-front passage. A strong dry air mass is observed between 400 and 300 hPa. The surface heating during the day and the ejection of humidity by the SB-front and the northwest wind canalized by the frontal system during the afternoon (Figure 4(b)). This situation favored the increase of instability indices in an environment of weak vertical shear at 1800 UTC.

Figure 4(c) shows a mesoscale signature in the radial velocity field at 25 km away from the radar. A convergence region induced by SB-front (blue tone), and the northwest wind (red tone), is observed over the center of the MASP at 2025 UTC, highlighted area. The radial velocity measured of the flows is ~8 m·s^{-1}. The air mass flow associated with northwest wind associated with the jet (red tone),

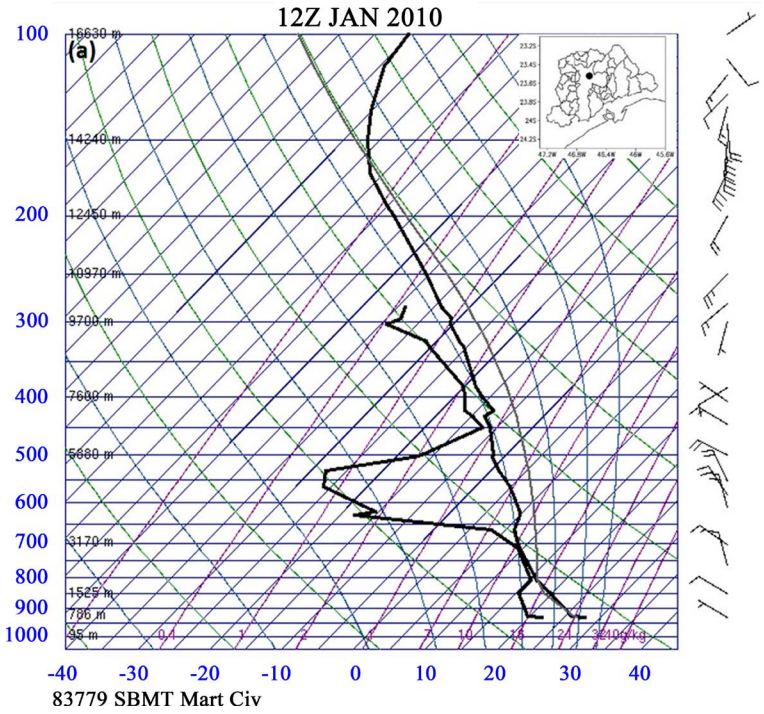

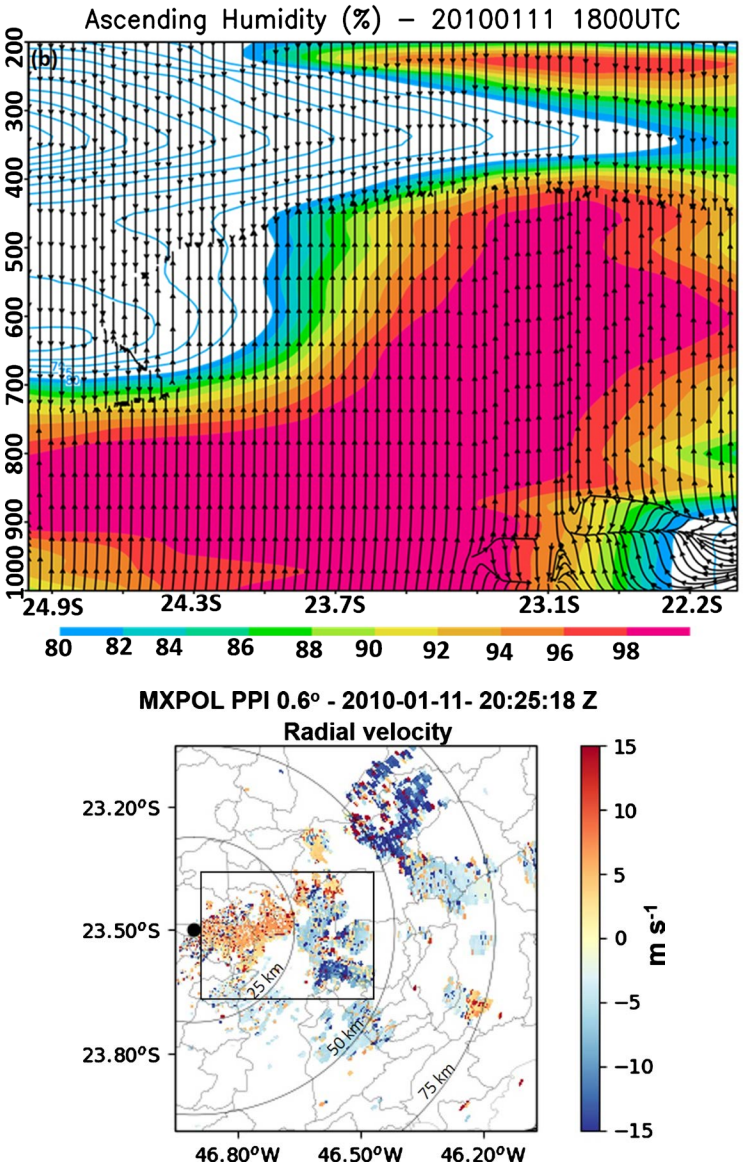

Figure 4. (a) The University of Wyoming Skew-T Log-P diagrams of the 1200 UTC on 11 January 2010 sounding in São Paulo City (23˚33.4'S; 46˚ 44.1'W). (b) The vertical profile of the relative humidity (%) from the reanalyzes of the ECMWF within a column 12.5 km × 12.5 km resolution at 47˚60'W between 22˚25'S to 24˚95'S at 1800 UTC (b) on 11 January 2010. (c) PPIs at 0.6˚ of radial velocity (Vr) at 2025 UTC on 11 January 2010. Color scale indicates radial velocities ($m \cdot s^{-1}$); blue (negative) and red (positive) tons are towards and away from MXPOL. The rectangle indicates the convergence signature below. Gray lines indicate geopolitical contours are indicated. The pressure scale is indicated as well as wind direction and intensity. The color scale indicates the relative humidity.

propagated against the SB-front (blue tone), triggering the convective cells over the center of São Paulo city.

3.3. Temporal Thunderstorm Evolution

Figure 5 shows PPIs 0.6˚ elevation of the reflectivity fields at (a) 1753 UTC, (b) 1850 UTC, (c) 1940 UTC, (d) 1955 UTC, (e) 2015 UTC, (f) 2025 UTC, (g) 2040

UTC, (h) 2050 UTC, (i) 2105 UTC, (j) 2115 UTC and (k) 2155 UTC on 11 January 2010. The reflectivity fields were obtained at a 5min time interval and animated to identify the sea breeze entering the MASP.

A very fine line of reflectivity between 0 dBZ and 10 dBZ at the 40-km range almost perpendicular to 150 ˚azimuth (inside the rectangle) was moving towards MXPOL, indicated by a black arrow (**Figure 5(a)**). It is the SB-front and its effect on convection over MASP. The SB-front intensifies as it spreads to the center of MASP. It shows PPI 0.6 ˚elevation of unfiltered reflectivity fields at 1753 UTC, 1850 UTC, 1940 UTC, 1955 UTC, 2015 UTC, and 2025 UTC, when the SB-front reaches the geometrical center of the RMSP, it presents an asymmetric configuration induced by the intense UHI in the region (**Figure 5(d)**). The low elevations PPIs of **Figure 4(b)** is passing through the large sensible heat storage within the urban canopy, where the first cell convection trigger at the eastern extreme of São Paulo city (1850UTC), which later moves out of São Paulo city (1940 UTC). At 1955UTC, the incoming SB-front interacts with the MASP UHI over the center of the São Paulo city and it stagnates temporarily over the center of São Paulo center, triggering convective cells in its rear (**Figure 5(d)**).

Figure 5(e) shows the convective cells with larger dimensions located towards northeast and east MXPOL at 2015UTC. These cells produced gust fronts, and these moved along the SB-front and triggered secondary convective cell (highlighted in the circle) intensifying and interconnecting the old cells at 2025UTC (**Figure 5(f)**). It is the beginning of the production of very deep convection with heavy rainfall, gusty winds, and lightning over the MASP geometrical center. **Figure 4(g)** shows an intense convective cell parallel to the region where the SB-front was stagnant 45 min earlier. This convective cell produces a gust front, a fine line of reflectivity between 20 dBZ and 25 dBZ which propagates toward MXPOL at 2040UTC (**Figure 5(g)**).

Figure 5(h) shows the unique cell thunderstorm, resulting from the aggregation of several cells. It observed the thunderstorm with asymmetric configuration induced by the intense UHI in the MASP geometrical center and also shows that the south end of the thunderstorm interacts directly with the SB-front. The fine line of reflectivity between 20 dBZ and 25 dBZ is the gusts of wind. These gusts of wind resulted from microburst which causing the cold pool to spread in all directions on the surface at 2050UTC and 2105UTC (**Figure 5(h)**, **Figure 5(i)**).

The SB-front was already outside of the study area (**Figure 5(i)**). The convective cell continues to produce gust front witch moving towards MXPOL, but without triggering new cells due to the absence of the SB-front on-site at 2105 UTC and 2115 UTC (**Figure 5(j)**). It is also observed that the thunderstorm loses the asymmetrical configuration. Therefore, the thunderstorm began to weaken, with a predominance of a stratiform system from 2135 UTC (Figure note show) to 2155 UTC (**Figure 5(k)**).

In the highlighted area of **Figure 6(f)**, we have the Zdr values, where green tones (Zdr ~ 3.2 dB) are noted, which indicates the presence of large drops

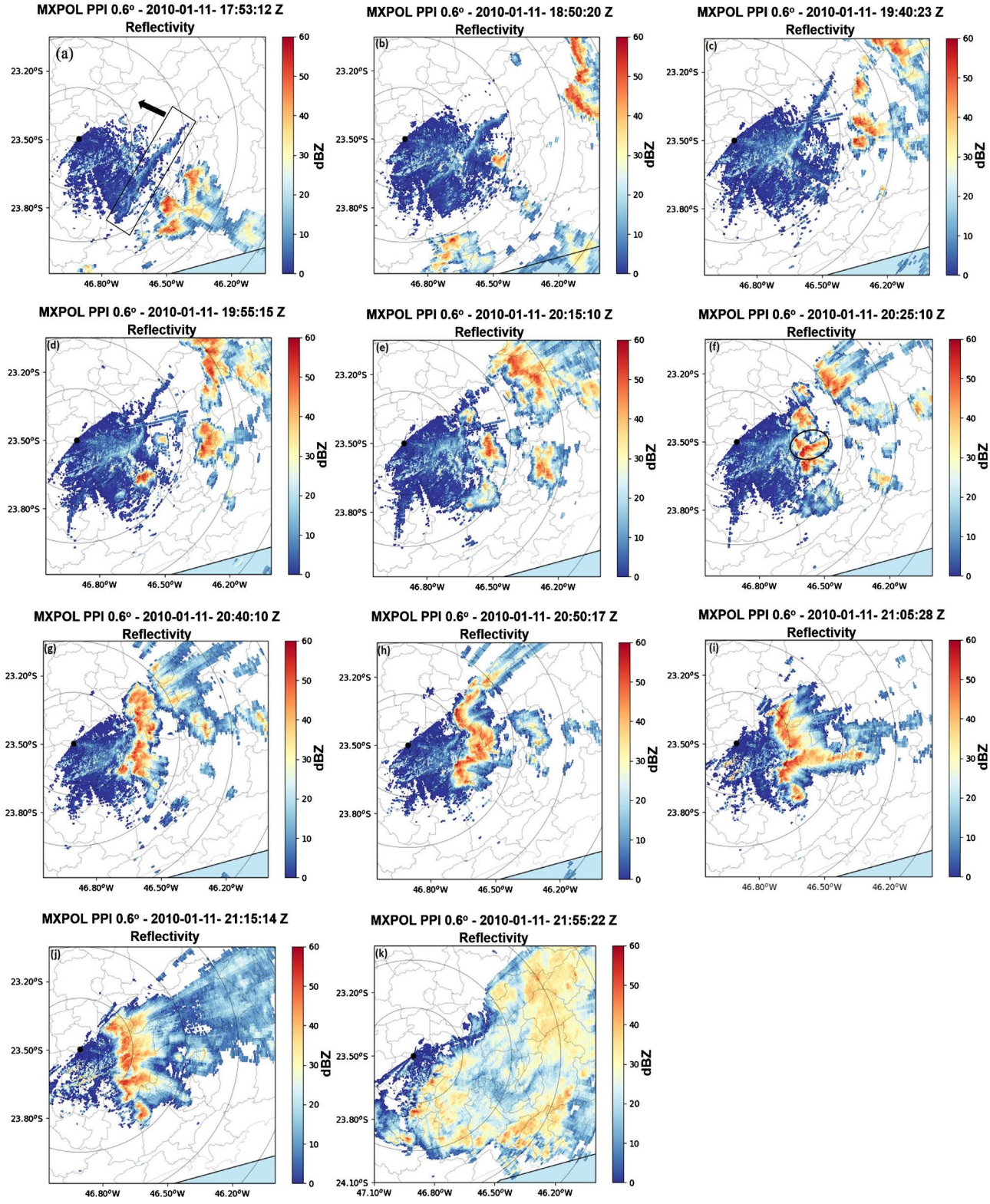

Figure 5. PPIs at 0.6˚ elevation of reflectivity (Z_H) at (a) 1753 UTC, (b) 1850 UTC, (c) 1940 UTC, (d) 1955 UTC, (e) 2015 UTC, (f) 2025 UTC, (g) 2040 UTC, (h) 2050 UTC, (i) 2105 UTC, (j) 2115 UTC and (k) 2155 UTC on 11 January 2010. Color scale indicates reflectivity (dBZ). The thin reflectivity line inside the rectangle is the sea breeze front. The black arrow indicates the displacement direction of the sea breeze front. MXPOL centered circumferences at $\Delta r = 25$ km. The black dot in the center of the smallest circle indicates the MXPOL position. Scale, Geographic contours, and UTC times are indicated.

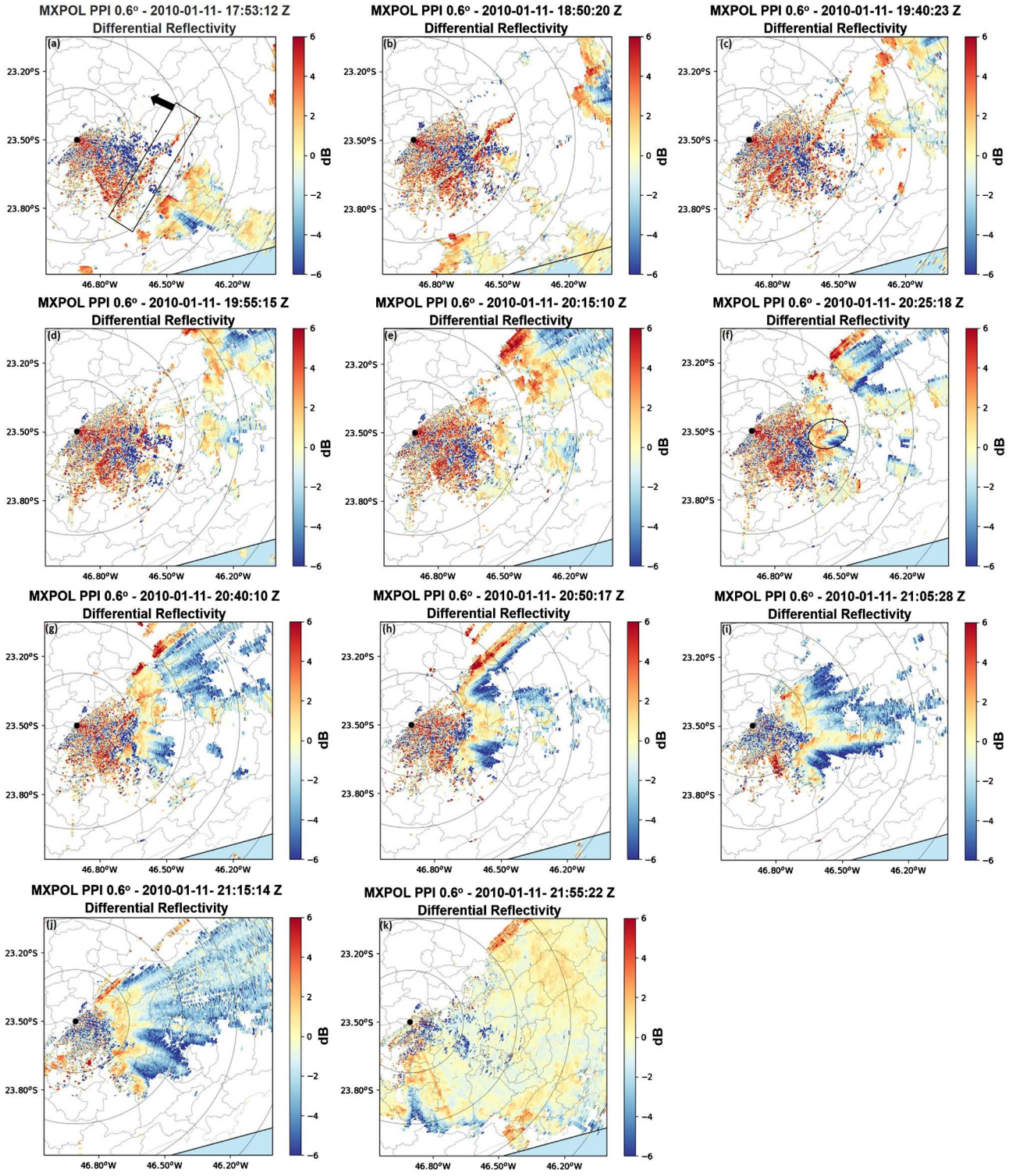

Figure 6. Idem **Figure 5** but for differential reflectivity.

between 1 mm and 5 mm in the two secondary cells incorporated. In the highlighted area, **Figure 5(f)**, the reflectivity field presents values > 55 dBZ. **Figure 7** shows the correlation coefficient that indicates all the cloud boundary areas felling the convective cells, and the storm cloud resulting from the incorporation of the

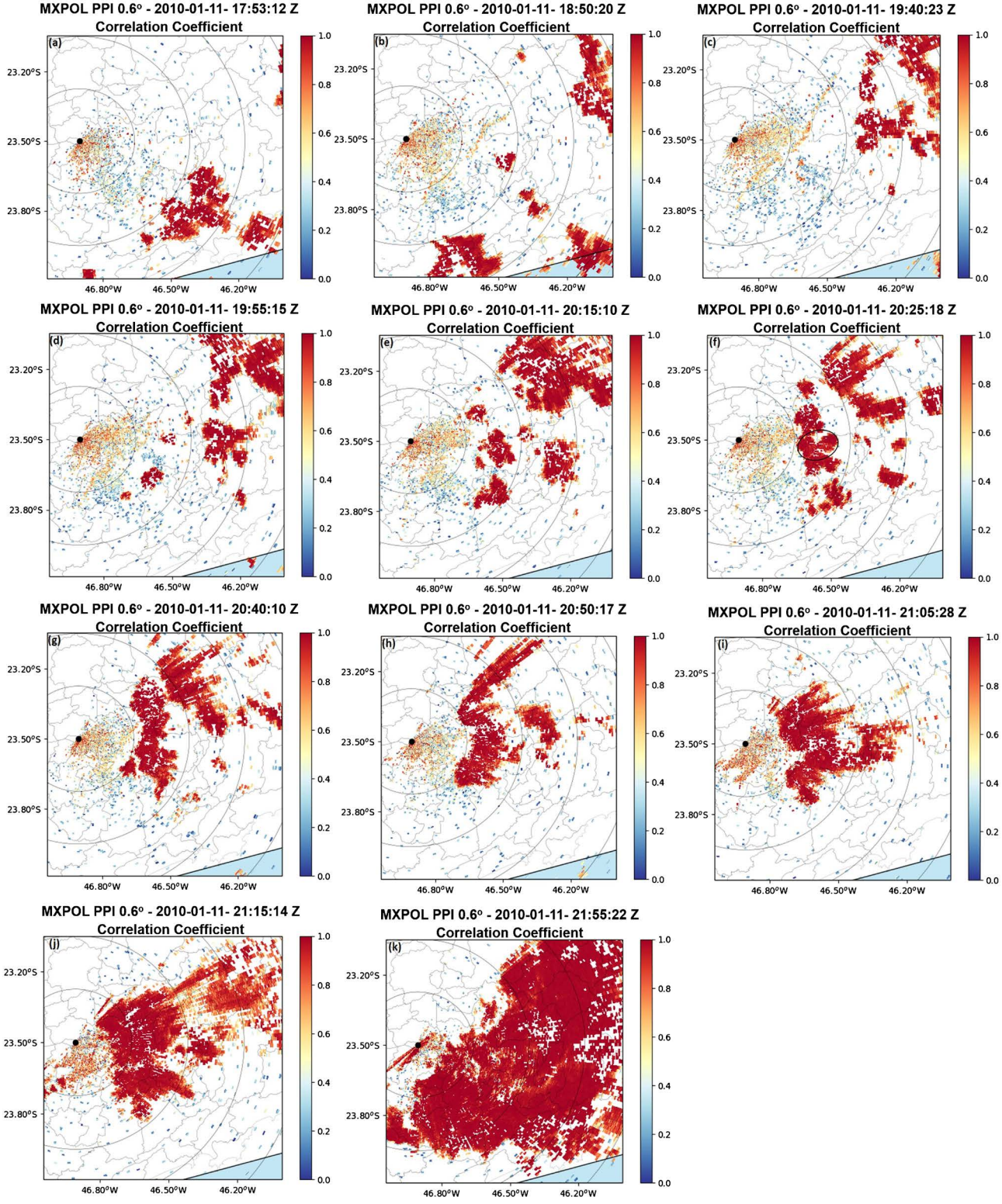

Figure 7. Idem **Figure 5** but for the Correlation coefficient.

secondary convective cells. **Figure 8** shows the specific differential reflectivity, where the most positives values indicate more intense rainfall areas with a predominance of oblate raindrops.

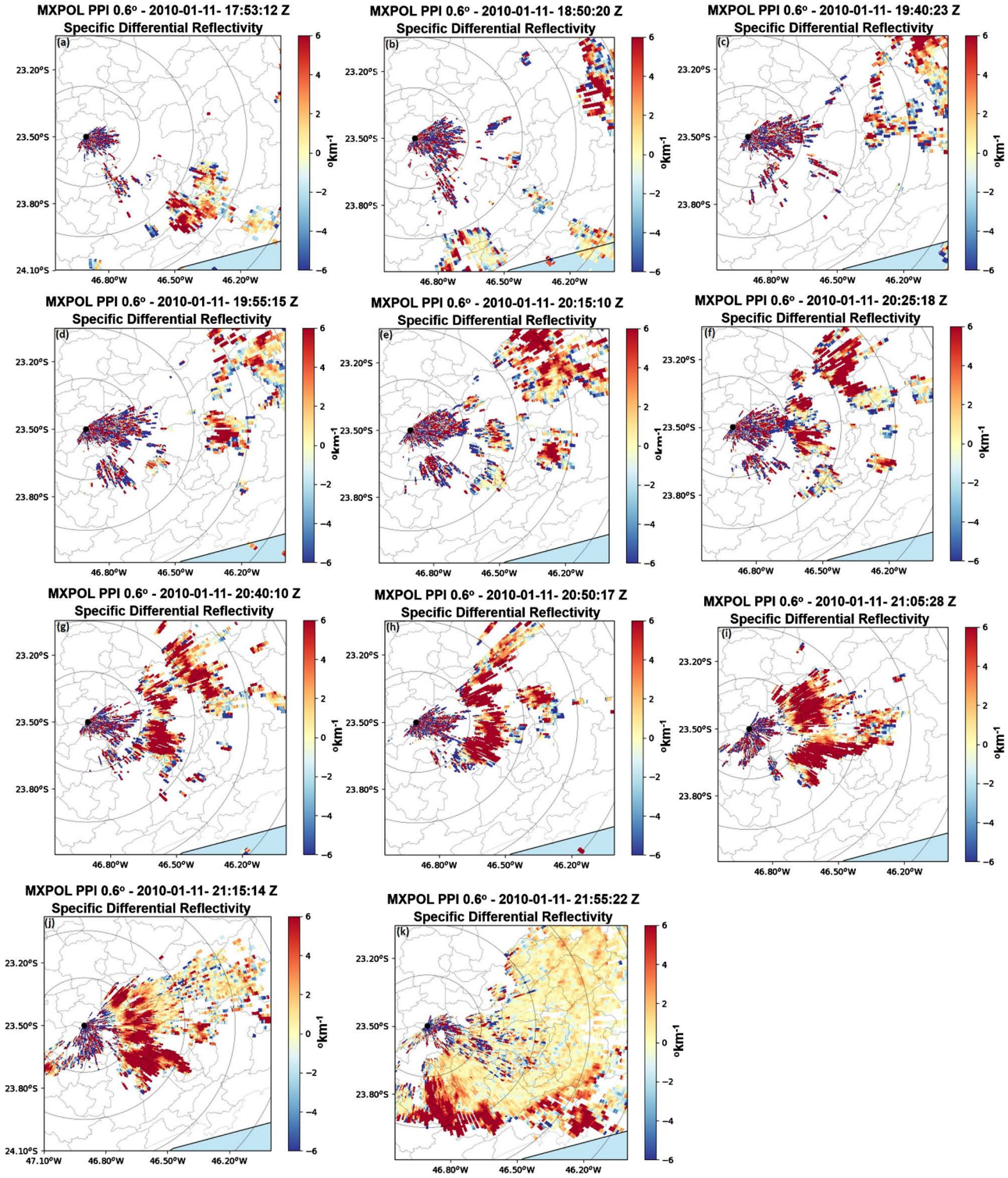

Figure 8. Idem **Figure 5** but for Specific differential reflectivity.

3.4. Hydrometeor Classification (HC), Liquid Water Mass, Liquid Ice mass, and Drop Spectrum

- High hail concentration in the secondary cell

Figure 9 show the high elevation PPIs (above the 0˚C isotherm) of hydrometeor

classification, reflectivity, differential reflectivity, specific differential reflectivity, liquid water mass, liquid ice mass, and drop diameter through the intense convective cell resulting from the feedback between the gust fronts of the first convective cells with SB-front, which caused the secondary cell trigger which caused greater hail production than other thunderstorm over the São Paulo city center.

The convective cell exhibited reflectivity values above 55 dBZ at freezing temperatures (**Figure 9(b)**, in the highlighted area). In the highlight of **Figure 9(c)**, **Figure 9(d)**, and **Figure 9(g)**, we have the differential reflectivity, specific differential reflectivity, and drop diameter values, where red tones (Z_{DR} between −0.5 and 2 dB, and K_{DP} between 0.5˚ and 6˚ km^{-1}) and drop diameters between 1 and 2 mm are noted, which indicates the presence of large drops and hail.

The highlight in **Figure 9(e)** indicates liquid water mass in the convective cell and ice mass with very high values at this altitude for liquid water (between 2.5

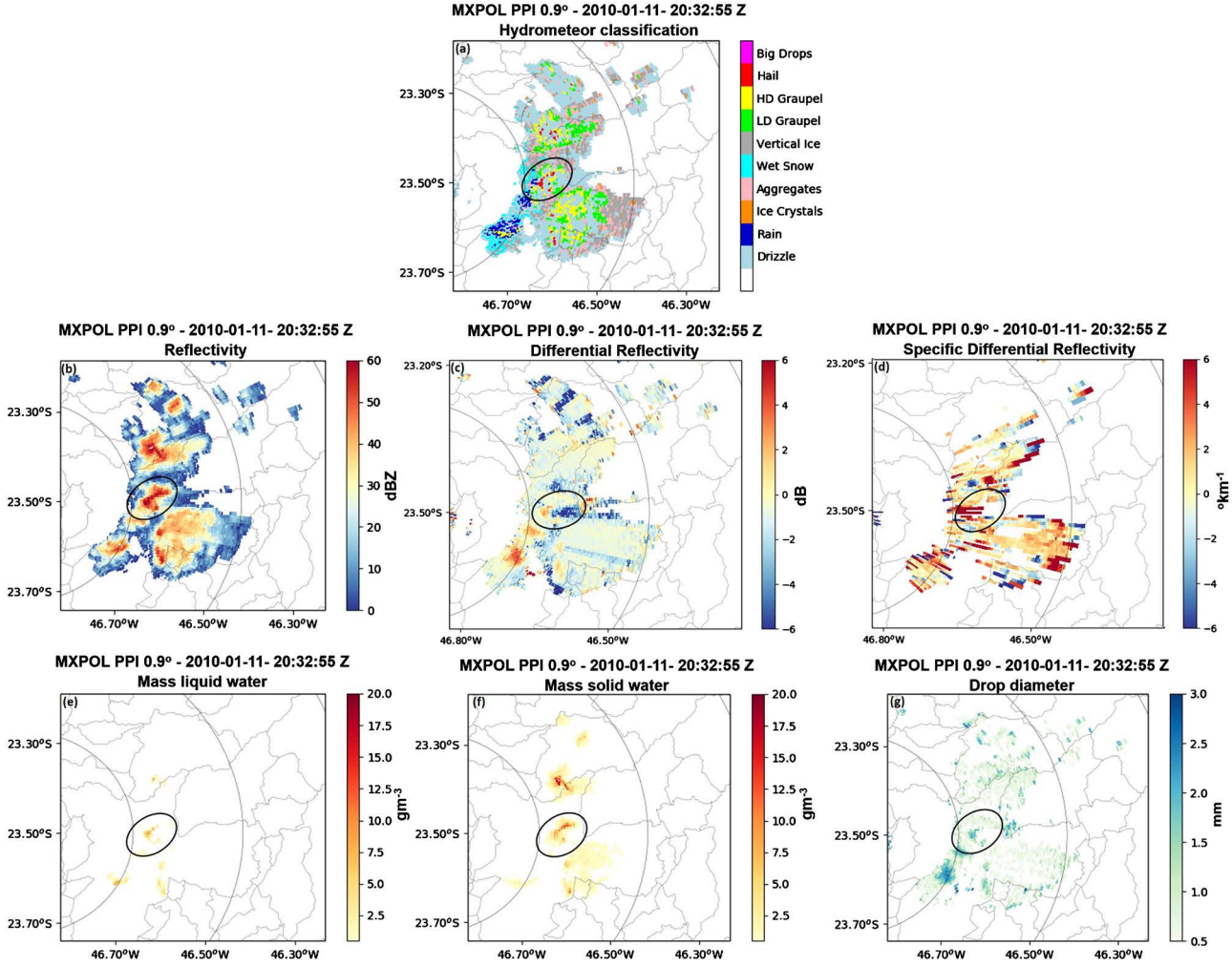

Figure 9. PPIs at 9.0˚ of (a) hydrometeor classification (HC), (b) reflectivity (Z_H), (c) differential reflectivity (Z_{DR}), (d) specific differential reflectivity (K_{DP}), (e) liquid water mass (f) liquid ice mass and (g) drop diameter at 2032 UTC on 11 January 2010. In the highlighted area, is the intense convective cell resulting from the integration of two secondary convective cells. MXPOL centered circumferences at Δr = 25 km. Scale, Geographic contours, and UTC times are indicated. Hydrometeor types, reflectivity (dBZ), differential reflectivity (dB), specific differential reflectivity (km^{-1}), water, and ice masses (g·m^{-3}) in color scales.

and 7.5 gm^{-3}), and the highlight in Figure 8(f) indicates high ice mass concentration (between 5 and 12.5 gm^{-3}).

Figure 9(a) indicates the hydrometeor classification and in the highlighted area is the region with the highest hail concentration of the precipitating system which is in agreement with the values of the polarimetric variables and the reflectivity.

The dynamics of strong convergence over the center of the São Paulo City was the cause of these peculiar microphysical characteristics. When hot-humid air associated with urban pollution over the center of São Paulo City is loaded to the cloud at negative temperatures, water vapor condenses producing a high amount of droplets and latent heat performed in the cloud. This increased instability and intensified the convergence of air masses of different properties (Figure 4(c)), which carried a high amount of water drops at negative temperatures.

- Strong downdrafts

Figure 10 shows the lower elevation (0.6˚) PPIs of hydrometeor classification, reflectivity, differential reflectivity, specific differential reflectivity, correlation coefficient, liquid water mass, liquid ice mass, and drop diameter of the storm's mature stage resulting from the integration of secondary convective cells over MASP.

Note that the storm presents an asymmetric configuration similar to the SB front caused by the intense convergence at low levels induced by the strong UHI in the São Paulo city center. The rectangular highlight in Figure 10(b) indicates the gust front caused by the storm. The frontal part of the storm presented reflectivity values above 55 dBZ (Figure 10(b)). Higher values (Z_H ~60 dBZ) are noted in the highlighted oval area in Figure 10(b). In the highlight oval areas of Figure 10(c) and Figure 10(d), there are the Z_{DR} and K_{DP} values, where are noted tones of red (Z_{DR} ~3.2 dB and K_{DP} ~6˚km^{-1}) that indicate the presence of large drops. The HC presented in Figure 10(a) (highlighted oval area) indicates rain mixed with big drops and hail probably reaching the surface, corresponding to the Z_H fields presenting intense nuclei ~60 dBZ, highlighted oval area.

Figure 10(e) shows the correlation coefficient indicating the entire cloud boundary area which encompasses the storm. In the oval highlight of Figure 10(h), we have the values of the raindrop diameters, where we notice darker tones of blue (~3 mm) which indicates the presence of large raindrops in the storm. Figure 10(f) shows a high concentration of liquid water mass perceptible, indicating areas of heavy rainfall. Figure 10(g) shows low ice mass concentration at low levels.

The hydrometeors classified in the PPI 0.6 ˚elevation in Figure 10(a), are the same as those observed in the PPIs 3.0 ˚elevation in Figure 11(a), characteristic of the collapse of the liquid water mass and solid water mass from the upper part from the cloud to the surface as observed highlighted areas. This aspect is characteristic of a microburst (Figure 10(a)), highlighted area. It is also observed reflectivity between 20 and 25 dBZ within concentric associated with the cold

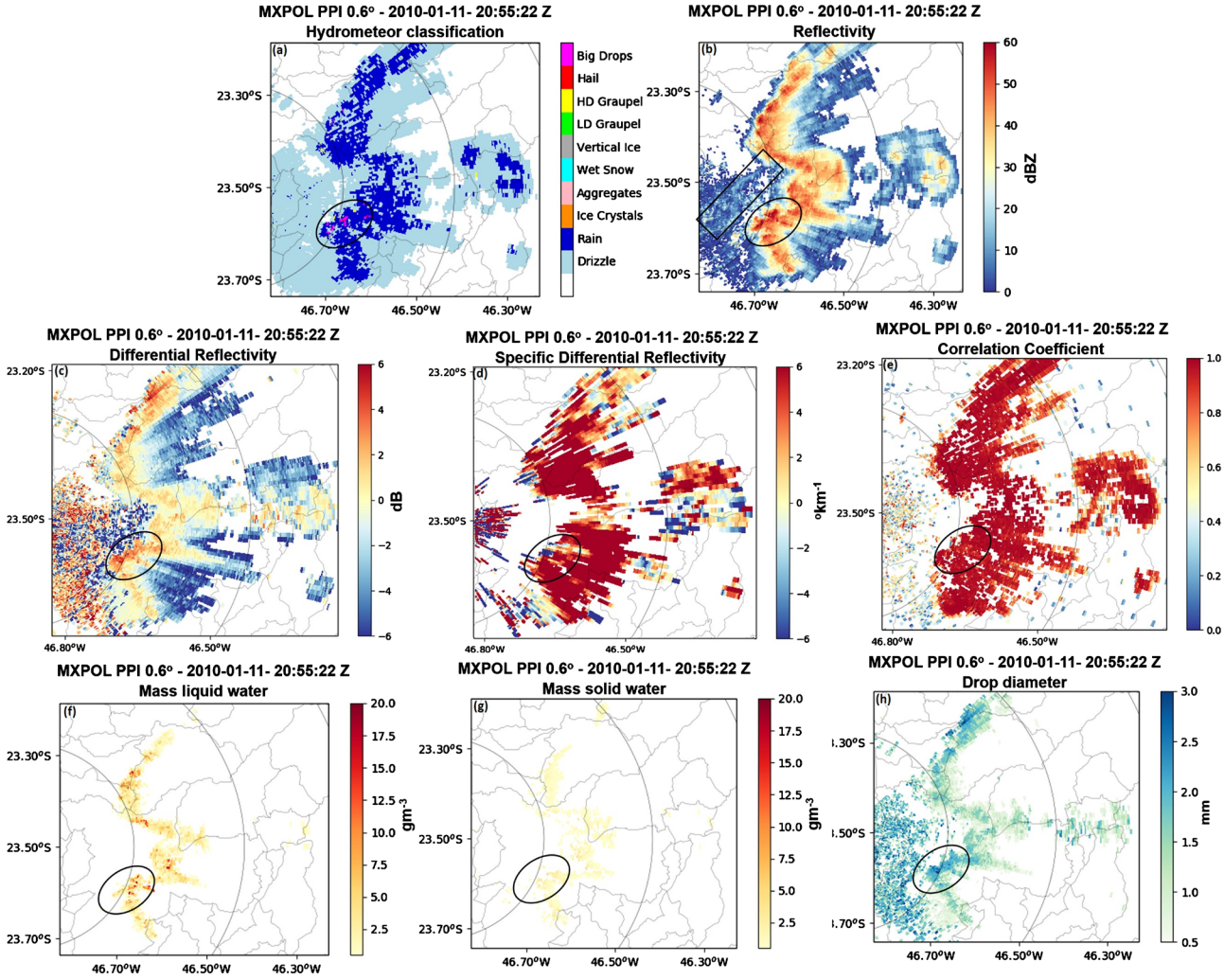

Figure 10. PPIs at 0.6˚ of (a) hydrometeor classification (HC), (b) reflectivity (Z_H), (c) differential reflectivity (Z_{DR}), (d) specific differential reflectivity (K_{DP}), (e) correlation coefficient (ρ_{HV}), (f) liquid water mass (g) liquid ice mass and (h) drop diameter at 2055 UTC on 11 January 2010. In the highlighted area, is observed mixture of rain, large drops, and hail is observed due to the probable occurrence of a microburst. MXPOL centered circumferences at $\Delta r = 25$ km. Scale, Geographic contours, and UTC times are indicated. Hydrometeor types, reflectivity (dBZ), differential reflectivity (dB), specific differential reflectivity (km^{-1}), correlation coefficient (without unity), water and ice masses ($g{\cdot}m^{-3}$) in color scales.

pool expelled by the gust front resulting from the strong downdrafts (Figure 10(b)).

The diameter of the raindrops (Figure 10(h) and Figure 11(h)) shows the concentration of drops of almost the same size at two different levels at the moment of collapse of liquid water mass and ice mass from cold thunderstorm region to surface at 2055 UTC. These results corroborate with DSD measured on the surface (Figure 12). Probably the DSD modification was caused by the collision-coalescence of big drops on cloud droplets, breakup by the collision between big drops, and breakup by aerodynamic force combined (Figure 10(h) and Figure 11(h)). This mechanism acted together to increase a large number of raindrops diameter from 0.551 to 1.116 mm (highlights 1 of Figure 12(a) and

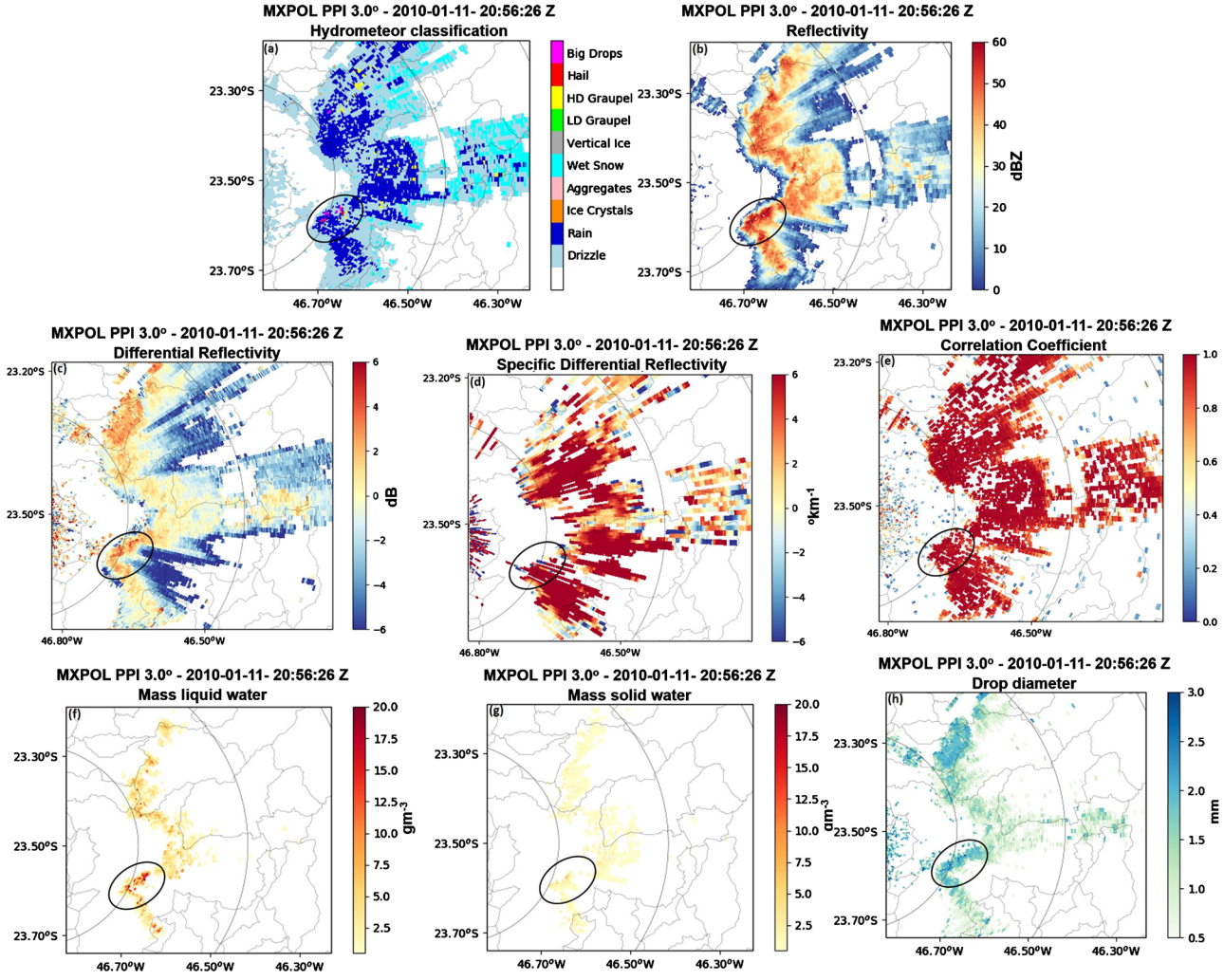

Figure 11. Idem Figure 10 but for PPIs at 3.0˚at 2056 UTC.

Figure 12(b)) and from 1.7 to 2.5 mm (highlights 2 of Figure 12(a) and Figure 12(b)).

Figure 12 shows the Time evolution of the numbers and size of raindrops of the storm in the mature and decay phases and Averaged drop size distributions estimated with JWD measurements of 76 rainfall storm from 1830 to 2100 on 11 JAN 2010. The sea breeze had just was over the JWD at 1753 UTC (Figure 4(a)). A first convective cell developed right above de JWD location at 1955 UTC (Figure 5(d)). JWD measurements of the main Storm with asymmetric and completely integrated configuration resulting from secondary convective cells started at 2050 UTC (Figure 5(h)). By 2155 UTC, the dominant rainfall was of the stratiform type (Figure 5(k)).

The time evolution of the drop spectra indicates the convective (in highlights 1 and 2), transition, and stratiform (in highlight 3) phases of the storm presenting raindrop diameters in all classes. It is interesting to note the high number of droplets estimated and the concentration of raindrops in highlights 1 and 2 of Figure 12(a) and Figure 12(b), and decrease in the number of larger diameter

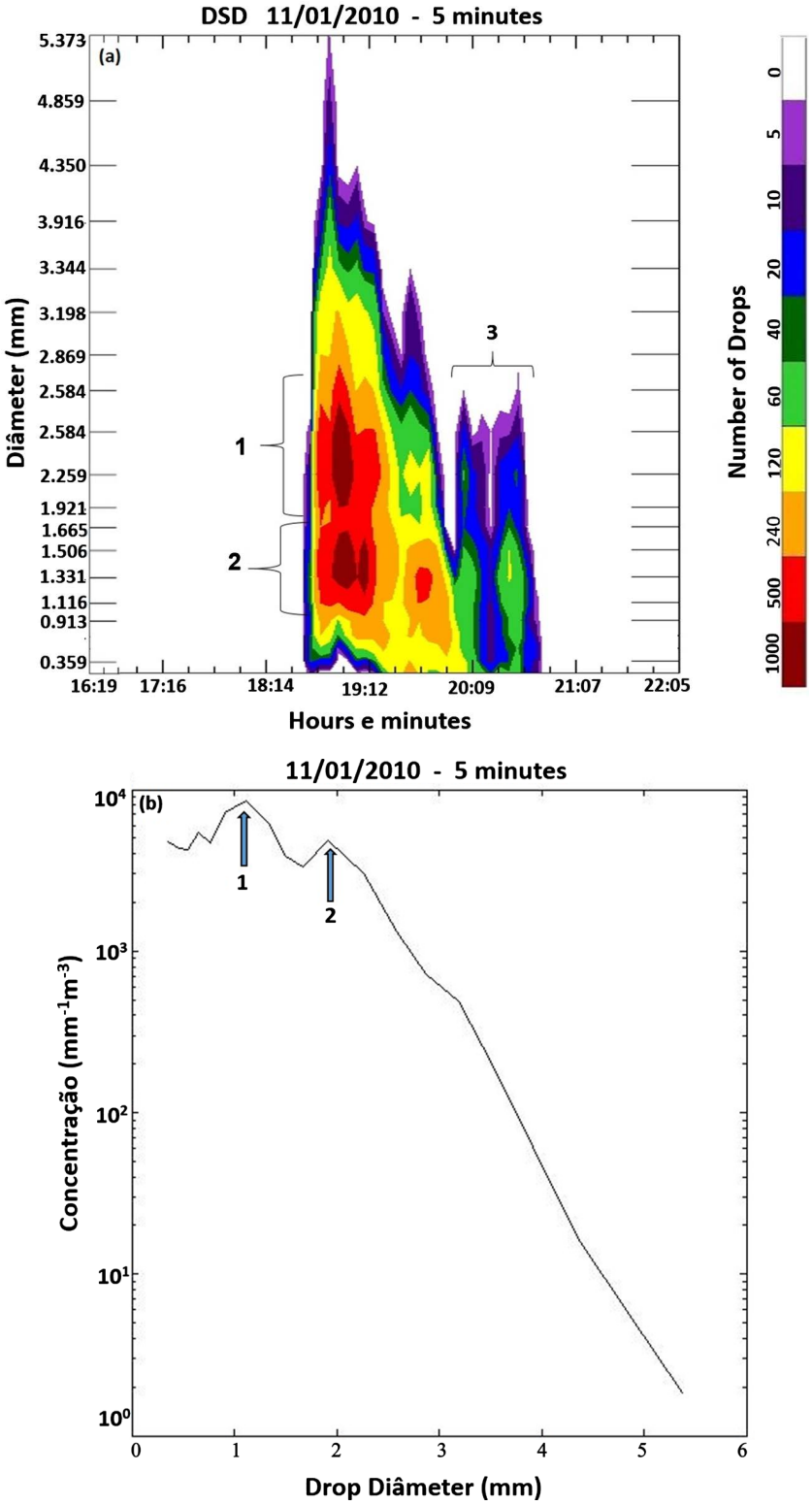

Figure 12. (a) Time evolution (LT) of JWD total number of drop sizes with diameters between 0.359 and 5.373 mm at PEFI (Figure 1) for the 11 JAN 2010 storm. (b) Averaged drop size distributions estimated with JWD measurements of 76 rainfall storms from 1830 to 2100 on 11 JAN 2010 at PEFI, São Paulo City (Figure 1). (a) Source: Adapted from [19].

raindrops and concentration of raindrops. It suggested that the injection of a deeper layer of moisture, as well as boundary layer shear, induces a higher drop concentration at all diameters. Furthermore, urban densification has impacted the increase of raindrop concentration.

4. Discussion

The fuzzy logic applied to MXPOL radar data as reflectivity, differential reflectivity, specific differential reflectivity, and the correlation coefficient was successfully performed to obtain the hydrometeors classification present in the thunderstorm. The attenuation was not corrected to the spatiotemporal evolution of the sea breeze front over MASP. However, this thunderstorm was intense and caused signal attenuation, and probably influenced the hydrometeors classification as graupel and hail. For the X-band radar still a case study under development for the hydrometeor classification consistency from an intense storm. Another aspect that may also have influenced hydrometeors classification is the altitude and temperature data. The sounding data from Campo de Marte Airport of São Paulo city at 1200 UTC were used the nearest to the event's occurrence. This event began at 1700 UTC, five (5) hours before the start of the event. Was also calculated the liquid water mass and ice mass, and raindrop diameter using the reflectivity and differential reflectivity.

The reflectivity fields showed primary and secondary cell triggers at the rear of the SB front as it propagated towards the geometric center of the MASP. These convective cells were aggregated when the SB front stagnated over the geometric center of MASP, forming a single convective cell (thunderstorm) with a north-south orientation over the São Paulo city.

The SB fronts tend to increase environmental shear and associated vorticity and moist and MASP urban aerosol convergence [2]. When the SB front and gust fronts of the primary cells collide there is a reduction of moist static stability and new convective cells initiate over MASP [6].

The UHI caused by urban densification at the geometric center of MASP induced strong convergence of southeast and northwest flow over São Paulo city center which blocked the advance of the SB front for almost2hours.TheMASP UHI is caused by large sensible heat storage within the urban canopy in the early hours of the day and released during the afternoon and night over the center of São Paulo [5]. This effect induced an asymmetric configuration of the SB front and the thunderstorm. Part of the southern end of the storm interacted directly with the stagnant SB front. Subsequently, the sea breeze progresses beyond the São Paulo city when the heat island probably dissipated, and the thunderstorm loses its asymmetrical configuration and sometime later begins to dissipate.

Environments with high aerosol concentration may favor the development of strong updrafts reaching high altitudes to the base of the tropopause, allowing the cloud to develop to this level [34]. The radial velocity fields show strong convergence at low levels over the São Paulo city center. Several authors [5] [6]

[11] have claimed that the SB front moves towards RMSP, where surface rugosity and UHI increase humidity convergence and upward movement, respectively.

A strong downdraft probably was also occurred at the southern end of the thunderstorm where the microphysical characteristics of the hydrometeors (big drops and hail) found after the base of the 0º C isotherm were the same found in the lower part of the thunderstorm. As observed by [35], observations of airplane sonice crystals in the cloud, suggest that the mechanism of production in the secondary droplet freezing process in ice production is in the strong updrafts that carry these droplets and operate for the formation of freezing nuclei. The consequence of this is the production of small ice particles colliding with supercooled droplets, which produce the hailstones within the strong updrafts [35], as observed in the results.

According to [20], as the ice mass precipitates below the 0˚C isotherm, part of the solid water mass thaws, providing the formation of big drops. According to some authors, for the thawing process to occur, energy is needed from the surrounding air with more hot temperatures [20]. The thawing process cools the air and causes cold air to accelerate downdrafts.

The results showed a high concentration of liquid water mass and ice mass of 12.5 gm^{-3} above the 0˚C isotherm in the area where the peculiar concentration of hail occurred. A high concentration of liquid water mass of ~17.5 gm^{-3} was also observed after the base of the 0˚C isotherm and in the lower part of the thunderstorm where the strong downdrafts occurred as well as the probable occurrence of microburst. But the concentration of ice mass varied, it was observed high concentration of the 5 gm^{-3} and a low concentration of 2.5 gm^{-3} after the base of 0˚C isotherm and a high concentration of 4 gm^{-3} in the lower part of the thunderstorm. According to [36] and [37], latent cooling performed or latent heat absorbed during freezing, evaporation, and sublimation negatively increases buoyancy, intensifying downdrafts. These processes are the cause of strong downdrafts for the occurrence of microburst [38]. As the volume of liquid water mass and solid water mass precipitates from the upper region of the cloud (as observed in the results), it drags the air together causing the cold pool in the surface.

The concentration of raindrop diameter also varied in the strong downdrafts probably occurred, there was a high concentration of >2.5 mm diameter raindrops in the lower part of the storm and a high concentration of >2 mm raindrops diameter after the base of the 0˚C isotherm. These results corroborated with those observed by JWD in the surface, where raindrops of 2,259 mm diameter were the fourth peak of the highest concentration of raindrops in DSD. Almost all surface rain during convective events comes from the melting of hail and graupel [39].

Almost 2 hours later the UHI dissipated, the SB front spread out of the São Paulo city and the thunderstorm loses its asymmetric configuration, entering the terminal life cycle. The MASP UHI effect accelerates the incoming SB front to-

wards the center of São Paulo, with the induced circulation slowing the SB front, leading to a strong convergence zone in the center of the city [7]. When its arrival in the urban region, the SB front stalls over the center of the city for about 2h. Posteriorly, the SB progresses beyond the city when the UHI dissipates [7].

5. Conclusions

The thunderstorm resulted from the simultaneous interaction of a cold front, low-level jets (northwest flow), sea breeze circulation and large urban area (with heat island) over the MASP.

The urban densification (and heat island) in São Paulo city centre induced strong convergence of the air masses of the sea breeze circulation and of the low level jet (northwest), and prevents the advance of the SB front for almost 2 hover the region.

The interaction of the sea breeze front, gust fronts, and the urban densification of São Paulo city center caused triggers of the most intense secondary cell in the rear of the breeze front and resulted in a peculiar microphysics with higher hail production above the 0°C isotherm than other areas of the thunderstorm.

The mesoscale system (sea breeze circulation) and synoptic scale (frontal system) would not be enough to cause an intense thunderstorm over the region. Anthropogenic action (urbanized areas and heat island) is the main factor for the formation of violent storms over MASP.

These important microphysical processes within long-lasting secondary convective cells should be taken into account on convective parameterization schemes as well as the associated cold pool dynamics.

Acknowledgements

The authors would like to thank IAG and INPE for providing datasets used in this work. They also would like to thank Colorado State University for providing the CSU radar tools software package used in the paper that is available at https://github.com/CSU-Radarmet/CSU_RadarTool. The CPTEC/INPE satellite images can be obtained at http://satelite.cptec.inpe.br. The sounding data are available at http://weather.uwyo.edu/upperair/sounding.html. This research and MXPOL were sponsored by The State of São Paulo Research Support Foundation (FAPESP) under grant 13952-2, and by CAPES (Finance code 001). A.J.P.F is supported by Conselho Nacional de Desenvolvimento Científico e Tecnológico—CNPq under grant 301149/2017-8.

Conflicts of Interest

The authors declare no conflicts of interest regarding the publication of this paper.

References

[1] Rojas, J.L.F., Pereira Filho, A.J., Karam, H.A., Vemado, F. and Masson, V. (2018)

Effects of Explicit Urban-Canopy Representation on Local Circulations above a Tropical Mega-City. *Boundary Layer Meteorology*, **166**, 83-111. https://doi.org/10.1007/s10546-017-0292-8

[2] Pereira Filho, A.J., Massambani, O., Martins, P. and Cazenave, F. (2007) An Operational Mobile XPOL for Hydrometeorological Applications in Brazil. 33*rd Conference on Radar Meteorology*, Cairns, 5 August 2007, Paper P10.14.

[3] Ferreira, M.J., de Oliveira, A.P. and Soares, J. (2011) Anthropogenic Heat in the City of São Paulo, Brazil. *Theoretical and Applied Climatology*, **104**, 43-56. https://doi.org/10.1007/s00704-010-0322-7

[4] Pereira Filho, A.J. (2012) A Mobile X-POL Weather Radar for Hydrometeorological Applications in the Metropolitan Area of São Paulo, Brazil. *Geoscientific Instrumentation, Methods, and Data Systems*, **1**, 169-185. https://doi.org/10.5194/gi-1-169-2012

[5] Pereira Filho, A.J., Vemado, F., Saito, K., Seko, H., Rojas, J.L.F. and Abi Karam, H. (2018) ARPS Simulations of Convection during TOMACS. *Journal of the Meteorological Society of Japan, Ser.* II, **96A**, 247-263.

[6] Hallak, R. (2007) Simulações numéricas de tempestades severas na RMSP. Ph.D. Thesis, Department of Atmospheric Science, University of Sao Paulo, São Paulo.

[7] Freitas, E.D., Rozoff, C.M., Cotton, W.R. and Dias, P.L.S. (2007) Interactions of an Urban Heat Island and Sea-Breeze Circulations during Winter over the Metropolitan Area of São Paulo, Brazil. *Boundary-Layer Meteorology*, **122**, 43-65. https://doi.org/10.1007/s10546-006-9091-3

[8] Bourscheidt, V., Pinto Jr., O. and Naccarato, K.P. (2016) The Effects of Sao Paulo Urban Heat Island on Lightning Activity: Decadal Analysis (1999-2009). *Journal of Geophysical Research: Atmospheres*, **121**, 4429-4442. https://doi.org/10.1002/2016JD024782

[9] Pereira Filho, A.J., Barros, M.T.L., Hallak, R. and Gandu, A.W. (2016) Enchentes na regiao metropolitana de São Paulo: Aspectos de mesoescala e avaliação de impactos. 13*th Brazilian Congress Brasileiro of Meteorology*, Fortaleza, September 2016, 28-93.

[10] He, G.X., Yu, C.W.F., Lu, C. and Deng, Q.H. (2013) The Influence of Synoptic Pattern and Atmospheric Boundary Layer on PM10 and Urban Heat Island. *Indoor and Built Environment*, **22**, 796-807. https://doi.org/10.1177%2F1420326X13503576

[11] Vemado, F. and Pereira Filho, A.J. (2016) Severe Weather Caused by Heat Island and Sea Breeze Effects in the Metropolitan Area of São Paulo, Brazil. *Advances in Meteorology*, **2016**, Article ID 8364134. https://doi.org/10.1155/2016/8364134

[12] Pereira Filho, A.J., Vemado, F., Peres, J.R., Silva Jr., I.W. and Tanaka, K. (2013) Measurements of Drop Size Distribution in a Megacity. *American Meterological Society*, **Section 2A. 3**, 1-5. https://ams.confex.com/ams/36Radar/webprogram/Paper228510.html

[13] Oliveira, A.P. and Dias, S. (1982) Aspectos observacionais da brisa marítima em São Paulo. *Anais Congresso Brasileiro de Metereologia*, **3**, 129-145.

[14] Nesbitt, S.W., Cifelli, R. and Rutledge, S.A. (2006) Storm Morphology and Rainfall Characteristics of TRMM Precipitation Features. *Monthly Weather Review*, **134**, 2702-2721. https://doi.org/10.1175/MWR3200.1

[15] Gochis, D.J., Shuttleworth, W.J. and Yang, Z.L. (2002) Sensitivity of the Modeled North American Monsoon Regional Climate to Convective Parameterization. *Monthly Weather Review*, **130**, 1282-1298. https://doi.org/10.1175/1520-0493(2002)130%3C1282:SOTMNA%3E2.0.CO;2

[16] Wang D., Yin J. and Zhai G. (2002) *In-Situ* Measurements of Cloud-Precipitation Microphysics in the East Asian Monsoon Region since 1960. *Journal of Meteorological Research*, **29**, 155-179. https://doi.org/10.1007/s13351-015-3235-7

[17] Kraut, I. (2015) Separating the Aerosol Effect in Case of a "Medicane" (Vol. 68). KIT Scientific Publishing. https://doi.org/10.5445/KSP/1000047813

[18] Bauer, P., Thorpe, A. and Brunet, G. (2015) The Quiet Revolution of Numerical Weather Prediction. *Nature*, **525**, 47-55. https://doi.org/10.1038/nature14956

[19] Pereira Filho, A.J., Barros, M.T.L., Hallak, R. and Gandu, A.W. (2013) Measurements of Drop Size Distribution in a Megacity. 36*th Conference on Radar Meteorology*, Breckenridge, 6-20 September 2013, 28-93.

[20] Rinehart, R.E. (2010) Radar for Meteorologists: Or You, too, Can Be a Radar Meteorologist III. In: Rinehart, R.E., Ed., *Radar for Meteorologists*, 4th Edition, Rinehart Publications, Columbia, 482.

[21] Silva, T., Beneti, C., Siqueira, P., Buzzi, M. and Calvetti, L. (2017). Severe Weather Identification Using Polarimetric Radar and Machine Learning Techniques. 38*th Conference on Radar Meteorology*, *AMS,* Chicago.

[22] Fabry, F. (2015) Radar Meteorology: Principles and Practice. Cambridge University Press, Cambridge. https://doi.org/10.1017/CBO9781107707405

[23] Kumjian, M. (2013) Principles and Applications of Dual-Polarization Weather Radar. Part I: Description of the Polarimetric Radar Variables. *Journal of Operational Meteorology*, **1**, 226-242. https://doi.org/10.15191/nwajom.2013.0119

[24] Ruzanski, E. and Chandrasekar, V. (2012) Nowcasting Rainfall Fields Derived from Specific Differential Phase. *Journal of Applied Meteorology and Climatology*, **51**, 1950-1959. https://doi.org/10.1175/JAMC-D-11-081.1

[25] Vivekanandan, J., Zrnic, D.S., Ellis, S.M., Oye, R., Ryzhkov, A.V. and Straka, J. (1999) Cloud Microphysics Retrieval Using S-Band Dual-Polarization Radar Measurements. *Bulletin of the American Meteorological Society*, **80**, 381-388. https://doi.org/10.1175/1520-0477(1999)080%3C0381:CMRUSB%3E2.0.CO;2

[26] Lang, T., Dolan, B., Guy, N., Gerlach, C. and Hardin, J. (2019) CSU-azxRadarmet/CSU RadarTools: CSU RadarTools v1.3.

[27] Helmus, J.J. and Collis, S.M. (2016) The Python ARM Radar Toolkit (Py-ART), a Library for Working with Weather Radar Data in the Python Programming Language. *Journal of Open Research Software*, **4**, Article No. e25. https://doi.org/10.5334/jors.119

[28] Dolan, B. and Rutledge, S.A (2009) A Theory-Based Hydrometeor Identification Algorithm for X-Band Polarimetric Radars. *Journal of Atmospheric and Oceanic Technology*, **26**, 2071-2088. https://doi.org/10.1175/2009JTECHA1208.1

[29] Rauber, R.M. and Nesbitt, S.W. (2018) Radar Meteorology: A First Course. John Wiley Sons, Hoboken. https://doi.org/10.1002/9781118432662

[30] Heske, T. and Heske, J. (1996) "Fuzzy" Logic for Real World Design. Annabooks, Rancho Mirage, 428.

[31] Liu, H. and Chandrasekar, V. (2000) Classification of Hydrometeors Based on Polarimetric Radar Measurements: Development of Fuzzy Logic and Neuro-Fuzzy Systems, and in *Situ* Verification. *Journal of Atmospheric and Oceanic Technology*, **17**, 140-164. https://doi.org/10.1175/1520-0426(2000)017%3C0140:COHBOP%3E2.0.CO;2

[32] Cifelli, R., Petersen, W.A., Carey, L.D., Rutledge, S.A. and da Silva Dias, M.A. (2002) Radar Observations of the Kinematic, Microphysical, and Precipitation Characteris-

tics of Two MCSs in TRMM LBA. *Journal of Geophysical Research*: *Atmospheres*, **107**, LBA 44-1-LBA 44-16. https://doi.org/10.1029/2000JD000264

[33] Houze Jr., R.A. (2014) Cloud Dynamics. Vol. 104, Academic Press, Waltham.

[34] Khain, A., Rosenfeld, D. and Pokrovsky, A. (2005) Aerosol Impact on the Dynamics and Microphysics of Deep Convective Clouds. *Quarterly Journal of the Royal Meteorological Society*, **131**, 2639-2663. https://doi.org/10.1256/qj.04.62

[35] Lawson, R.P., Woods, S. and Morrison, H. (2015) The Microphysics of Ice and Precipitation Development in Tropical Cumulus Clouds. *Journal of the Atmospheric Sciences*, **72**, 2429-2445. https://doi.org/10.1175/JAS-D-14-0274.1

[36] Liu, C., Moncrieff, M.W. and Zipser, E.J. (1997) Dynamical Influence of Microphysics in Tropical Squall Lines: A Numerical Study. *Monthly Weather Review*, **125**, 2193-2210. https://doi.org/10.1175/1520-0493(1997)125%3C2193:DIOMIT%3E2.0.CO;2

[37] Szeto, K. and Stewart, R. (1997) Effects of Melting on Frontogenesis. *Journal of the Atmospheric Sciences*, **54**, 689-702. https://doi.org/10.1175/1520-0469(1997)054%3C0689:EOMOF%3E2.0.CO;2

[38] Fujita, T.T. and McCarthy, J. (1999) Radar in Meteorology. American Meteorological Society, Boston, 657-681.

[39] Lin, H.M. and Wang, P.K. (1997) A Numerical Study of Microphysical Processes in the 21 June 1991 Northern Taiwan Mesoscale Precipitation System. *Terrestrial Atmospheric and Oceanic*, **8**, 382-404. https://doi.org/10.3319/TAO.1997.8.4.385(A)

Abbreviations

The following abbreviations are used in this manuscript:
MASP—Metropolitan Area of São Paulo
UHI—Urban heat island
SB—sea breeze
CF—cold front
INMET—Instituto Nacional de Meteorologia
IR—Infrared
LBA—Large-Scale Biosphere-Atmosphere
CPTEC—Centro de Previsão de Tempo e Estudos Climáticos
DAS—Satellite Division and Environmental Systems
INPE—Instituto Nacional de Pesquisas Espaciais
CAPE—Convective available potential energy
ECWMF—European Centre for Medium-Range Weather Forecasts
PPI—Plan position indicator
MXPOL—mobile X-band dual-polarization Doppler weather radar
dBZ—Stands for decibel relative to Z
UTC—Coordinated Universal Time
DSD—Drop size distribution
LT—Local time
Z—Reflectivity
ZDR—Differential reflectivity
KDP—Specific differential
ρHV—Correlation coefficient
DDP—Dual Doppler polarization
HC—Hydrometeors classification
MBF—Membership functions
ZDP—Reflectivity difference
MW—Liquid water mass
MI—Liquid ice mass
dB—Decibel
UD—Urban density
LD—Low density
HD—High density